Journal Name

ARTICLE TYPE

Engineering the kinetics and interfacial energetics of Ni/Ni–Mo catalyzed amorphous silicon carbide photocathodes in alkaline media†

Ibadillah A. Digdaya,[a] Paula Perez Rodriguez,[b] Ming Ma,[a] Gede W. P. Adhyaksa,[c] Erik C. Garnett,[c] Arno H. M. Smets,[b] and Wilson A. Smith*[a]

Photoelectrochemical (PEC) water splitting is a sustainable approach to produce a renewable fuel by harvesting the energy of the Sun to split water to form hydrogen and oxygen. In order to drive the water splitting reaction efficiently, substantial ohmic losses due to poor ionic conductivity of the electrolyte should be avoided, and therefore the reaction should be carried out at an extreme electrolyte pH. Herein we demonstrate the photoelectrochemical activity of an amorphous silicon carbide (a-SiC) photocathode for solar hydrogen evolution using an ultrathin nickel (Ni) film coupled with a nickel molybdenum catalyst (Ni–Mo) in a highly alkaline solution (pH 14). The incorporation of the Ni film coupled with Ni–Mo nanoparticles increases the number of active sites and therefore improves the kinetics of the hydrogen evolution reaction. Additionally, we report the influence of the catalyst configurations on the ohmic and solid liquid junction behavior on semiconducting interfacial layers. The a-SiC photocathode coated with the Ni/Ni–Mo dual-catalyst produces a photocurrent density of -14 mA cm^{-2} at 0 V *vs.* RHE using only cheap and abundant materials. This photocurrent is the highest recorded value from an amorphous-Si-based photocathode, and is achieved with a total film thickness of less than 150 nm.

Introduction

The global transition from fossil-based resources to renewable energy is critically important to address the sharply increasing threat of global climate change and to ensure long-term energy security. One attractive candidate to substitute for conventional fossil fuels is hydrogen. Hydrogen is an excellent energy carrier that can be directly converted into electricity *via* fuel cells, or combined with CO_2 or CO to form high energy density synthetic fuels. Most of the current industrial production of hydrogen, however, is *via* steam reforming of natural gas, which produces CO_2 as a by-product, making it environmentally unsustainable. Photoelectrochemical (PEC) water splitting, on the other hand, is a carbon-neutral alternative that is capable of converting and storing abundant solar energy into hydrogen using only renewable and clean resources. This process uses semiconductors to capture and convert sunlight into photogenerated charge carriers (*i.e.*, electrons and holes), and electrocatalysts to facilitate the multi-charge transfer process for the oxidation and reduction of water to oxygen and hydrogen, respectively.

Amorphous silicon (a-Si) has received considerable attention as a semiconducting photocathode, due to its strong absorption (up to 10^3 times stronger than c-Si) in the UV and visible part of solar spectrum and low temperature processing technique which allows large area thin film deposition on a wide variety of low-cost substrates.[1] Moreover, the optical band gap of a-Si can be controlled from 1.8 to 2.1 eV by incorporating carbon, forming amorphous silicon carbide (a-SiC),[2,3] thus giving extra versatility to establish a tandem PEC device with larger and/or smaller band gap photoabsorbers for maximum spectral utilization.

The main challenge of using amorphous Si-based materials as photoelectrodes is their poor stability in aqueous environments. However, this issue can be tackled by employing protection layers, such as titanium dioxide (TiO_2), which have been reported to be effective to stabilize c-Si photoelectrodes.[4–6] These protection strategies have also been demonstrated on a-Si and yield photocurrent onset potentials of $> +0.85$ V *vs.* RHE and photocurrent densities as high as -11.6 mA cm^{-2} at 0 V *vs.* RHE.[7,8] Similarly

[a] *Materials for Energy Conversion and Storage (MECS), Department of Chemical Engineering, Delft University of Technology, P.O. Box 5045, Delft 2600 GA, The Netherlands. E-mail: w.smith@tudelft.nl*
[b] *Photovoltaic Materials and Devices (PVMD), Department of Electrical Sustainable Energy, Delft University of Technology, P.O. Box 5031, Delft 2600 GA, The Netherlands.*
[c] *Center for Nanophotonics, FOM Institute AMOLF Science Park 104, Amsterdam 1098 XG, The Netherlands.*
† Electronic Supplementary Information (ESI) available.
See DOI: 10.1039/b000000x/

in our previous report we showed a thin film (100 nm absorber layer) of a-Si with 10% carbon incorporation (a-SiC) protected by amorphous TiO_2 producing an onset potential of +0.8 V *vs.* RHE with a photocurrent density of -8.3 mA cm^{-2} at 0 V *vs.* RHE at pH 4.[9] Although the lower photocurrent of our a-SiC can be attributed to its larger band gap (2 eV) than that of a-Si (1.8 eV), a-SiC photocathode has the potential to generate a higher photocurrent density up to -14 mA cm^{-2} at 0 V *vs.* RHE. The low performance of the previously reported a-SiC is likely due to the inability of the photocathode to rapidly rise the photocurrent at the onset potential as a direct consequence of the poor ionic conductivity of the near-neutral electrolyte at pH 4 that causes a large voltage drop across the Helmhotz plane. In order to minimize these substantial ohmic losses, it is therefore preferred to evaluate the photoelectrochemical performance of the a-SiC photocathode at an extreme pH.

In addition to the pH of the electrolyte, the inherent catalytic activity of the photocathode surface must be favorable to evolve hydrogen. While TiO_2 can effectively passivate the chemically unstable photocathodes, its surface is not active for the hydrogen evolution reaction (HER). Therefore, surface modification involving the incorporation of an active hydrogen evolving catalyst (HEC) is crucially required to enhance the kinetics of the surface reaction and lower the activation overpotential for the HER. Platinum (Pt) has been widely used as a catalyst due to its negligible thermodynamic and kinetic overpotentials for the HER. However Pt is scarce and expensive and might be impractical for large-scale production.[10] New classes of HEC's made from earth abundant materials, such as metal sulfides,[11–15] metal phosphides,[16,17] and metal carbides,[18,19] have recently emerged to be strong candidates that can act as cheap and efficient alternatives to substitute for Pt. However, similar to Pt, these catalysts are most catalytically active and stable only in acidic media.[20] When considering the overall water splitting reaction, both hydrogen and oxygen evolution need to take place simultaneously, and in many proposed configurations, in the same (photo)electrochemical cell. Therefore, considerations of stability and performance of the catalyst materials for water oxidation and reduction in a given electrolyte must be taken into account. Using an acidic electrolyte will leave noble-metal-based oxygen evolution reaction (OER) catalysts such as IrO_x and RuO_x as the only possible options as the counter electrode to evolve oxygen. However, cheap and abundant OER catalysts such as NiFeOOH are stable and work more efficiently in alkaline media.[21] Therefore, when envisioning a practical solar water splitting device that must operate in an extreme pH and considering the cost of materials, the most promising solution may be to operate the system in an alkaline electrolyte. Fortunately, several HER catalysts made from a wide selection of binary and ternary mixtures of Ni-alloys have recently demonstrated high activity and stability in strongly alkaline solutions.[22–25] Nickel-molybdenum (Ni–Mo) catalysts in particular have been reported to require less than 40 mV of overpotential to achieve a current density of -10 mA cm^{-2} in strong alkaline media for at least 24 hours.[26]

Despite enhancing the kinetics of the photoelectrochemical reaction, the surface catalyst may have a fundamental role on the semiconductor band-edge energetics and the charge transfer processes from the semiconductor to the electrolyte. We have previously demonstrated the energetics of a-SiC photocathodes coupled with a TiO_2 front surface layer which significantly influence the photovoltage of the isolated junction photocathodes.[9] However, the affect of the Ni–Mo catalyst on the interfacial electronic structure of the composite system was not further clarified since the catalyst was in the form of nanoparticles, thus still exposing the semiconductor surface to the electrolyte, and therefore was assumed to have no substantial impact on the energetics at the solid–liquid interface.

Herein we report the photoelectrochemical activity of a TiO_2-protected a-SiC photocathode coated with Ni–Mo nanoparticle catalysts in an alkaline solution. To further enhance the activity of the catalyst and to completely cover the surface, we deposited an ultrathin layer of Ni (2 nm) by radio frequency (RF) magnetron sputtering prior to the electrodeposition of Ni–Mo on TiO_2 coated a-SiC photocathodes. The incorporation of the thin layer of Ni increases the rate of hydrogen evolution, particularly at high applied cathodic potentials. The energetics between the TiO_2 interfacial layer and the catalyst were thoroughly investigated using electrochemical impedance spectroscopy (EIS). Finally, we demonstrate the functionalization of Ni/Ni–Mo dual catalysts that significantly increases the photoelectrochemical activity of the TiO_2 protected a-SiC photocathodes with a Ni counter electrode, resulting in a benchmark thin film photocurrent density of -14 mA cm^{-2} at the hydrogen evolution potential under 1 sun illumination using only cheap earth abundant materials.

Experimental section

Fabrication of a-SiC photocathodes

Hydrogenated amorphous silicon carbide (a-SiC) photocathodes were deposited onto textured fluorine-doped tin oxide (SnO_2:F, FTO) substrates (Asahi VU-type) using a radio frequency plasma enhanced chemical vapor deposited (RF-PECVD) multi-chamber tool. The substrate was kept at 170 °C during the deposition. An ultrathin (10 nm) boron doped hydrogenated amorphous silicon carbide (a-SiC(B)) was used as the p-type layer, decomposed from SiH_4 (20 sccm), CH_4 (45 sccm), and B_2H_6 (2 sccm) diluted gas flow under controlled pressure. The thin (100 nm) intrinsic a-SiC (SiH_4: 20 sccm, CH_4: 2.5 sccm, H_2: 170 sccm) was deposited in a separate chamber to avoid cross contamination. To complete the p–i–n structure, a thin (20 nm) n-type layer of phosphorus (P) doped nc-SiO_x (SiH_4: 2.5 sccm, CO_2: 2 sccm, PH_3: 1.2 sccm, H_2: 100 sccm). In our previous work we used an amorphous TiO_2 as the n-type layer, but here we found more consistent results when also depositing the n-type nc-SiO_x. An H_2 treatment in a low RF power density is followed in the same chamber in order to passivate the p–i–n interface. After the deposition, the p–i–n a-SiC is complete and a stripe of 300 nm Al was coated on the pre-covered FTO substrate area as the metal back contact using a Provac electron beam evaporator in rotation mode. Electrical contact was made using a silver wire attached by graphite paste.

Atomic layer deposition of TiO_2

Thin layers of amorphous TiO_2 (25 nm) were deposited onto the a-SiC photocathode or FTO glass substrate using a home-made thermal atomic layer deposition (ALD) system. The TiO_2 ALD was carried out at a substrate temperature of 200 °C using tetrakis(dimethylamino)-titanium (TDMAT) and H_2O as the Ti and O precursors, respectively. The pulsing times are 5 s and 10 ms for Ti and O, respectively. Each precursor was purged for 30 seconds after each pulse. The thickness of ALD TiO_2 was measured using spectroscopic ellipsometer (J.A. Woollam Co., Inc.) by depositing TiO_2 onto a Si wafer covered by its native oxide. The obtained data were fitted with the dieletric TiO_2 model and the growth rate per cycle was found to be 0.8 Å per cycle at deposition temperature of 200 °C. All samples were post-annealed in vacuum at 300 °C.

Catalyst depositions

An ultrathin Ni film was deposited using radio frequency (RF) magnetron sputter deposition in a Prevac sputter machine from a pure Ni target (99.95%). The Ar flow rate was 15 sccm and the power was 100 W. The Ni deposition time was 100 s, resulting in an approximately 2 nm think Ni film. The Ni–Mo catalyst was deposited using an electrodeposition technique using the recipe that has been described previously in another report,[27] except nickel sulfate was used instead of nickel sulfamate. The electrodeposition bath consisted of 1.3 M nickel(II) sulfate hexahydrate (Sigma-Aldrich, 99%), 0.5 M boric acid (Sigma-Aldrich, 99.5%) and 20 mM sodium molybdate dihydrate (Sigma-Aldrich, 99%). The pH of the solution was 5 and no pH adjustment was carried out. The Ni–Mo catalysts were potentiostatiocally deposited on the TiO_2 and the Ni coated TiO_2 at a fixed potential of -1.2 V *vs.* Ag/AgCl using a potentiostat (Parstat MC, Princeton Applied Research) until 1.0 C cm^{-2} of charge passed. The electrodeposition of Ni–Mo on the photocathodes was performed potentiostatically at -1.0 V *vs.* Ag/AgCl. During the deposition, the photocathodes were illuminated from the back side (*i.e.*, light hits the glass substrate first and then the photocathode) with the standard AM1.5 (1 sun) illumination (100 mW cm^{-2}) using a Newport Sol3A Class AAA solar simulator (type 94023A-SR3) with 450 Watt Xenon short arc lamp. Finally, the photocathodes were rinsed with milli-Q water before the photoelectrochemical measurements.

Photoelectrochemical measurements

The photoelectrochemical activity of a-SiC photocathodes was tested using a potentiostat (Parstat MC, Princeton Applied Research) in a three-electrode system, where the a-SiC photocathode with an exposed surface area of 0.28 cm^{-2} acts as the working electrode, a Ni coil acts as the counter electrode and an Ag/AgCl electrode (XR300, saturated KCL and AgCl solution, Radiometer Analytical) is used as the reference electrode. The potentials *versus* Ag/AgCl were converted to the reversible hydrogen electrode (RHE) using the following relationship:

$$V_{\mathrm{RHE}} = V_{\mathrm{Ag/AgCl}} + V^0_{\mathrm{Ag/AgCl\ vs\ NHE}} + 0.059\mathrm{pH} \quad (1)$$

where $V^0_{\mathrm{Ag/AgCl\ vs\ NHE}}$ is 0.199 V at 25 °C. The electrolyte used was 1 M potassium hydroxide (KOH) (Alfa Aesar, 85%) solution to obtain pH 14. Cyclic voltammetries were performed at a scan rate of 50 mV s^{-1} with 10 mV incremental steps. Photocurrents of a-SiC photocathodes were characterized under simulated AM1.5 solar irradiation (100 mW cm^{-2}) using a Newport Sol3A Class AAA solar simulator (type 94023A-SR3) with 450 Watt Xenon short arc lamp. The overall photoelectrochemical setup is sketched in Fig. 1. Gas product measurements of the samples were performed in a gas-tight electrochemical cell with an exposed active area of 0.785 cm^{-2}, using a gas chromatograph (GC, Interscience). The cell was continuously purged with a constant N_2 flow rate (20 sccm) and vented directly into the gas-sampling loop of the GC to enable periodic quantification of the gas-phase products. A thermal conductivity detector (TCD) was utilized to quantify hydrogen concentration. The Faradaic efficiency was determined by: $2n_{H_2}F/Q$, where n_{H_2} is the total amount of produced hydrogen (mol), F is the Faraday constant (96485 C mol^{-1}) and Q is the electric charge. The data were collected every 18 minutes and the current was integrated over the data collection time to calculate the Faradaic efficiency.

Electrochemical impedance spectroscopy

Electrochemical Impedance spectroscopy (EIS) measurements were performed on the bare TiO_2 (100 nm) substrates and with the catalyst coated TiO_2 substrates in a 1 M KOH electrolyte solution at pH 14 using a PARSTAT 4000 (Princeton Applied Research) potentiostat. During EIS measurements, the potential was scanned in the cathodic direction from +0.8 V to 0 V *vs.* RHE. The frequency range of measurement was 100 kHz to 0.1 Hz at a DC potential amplitude of 10 mV. The EIS data were fitted to equivalent electronic cicuits using the ZView® software (Scribner Associates). Mott–Schottky plots were obtained from the real capacitance values obtained by fitting the semicircles in the Nyquist plot, using a constant phase element instead of a perfect capacitor to account for non-ideal capacitive behaviors of the electrodes.

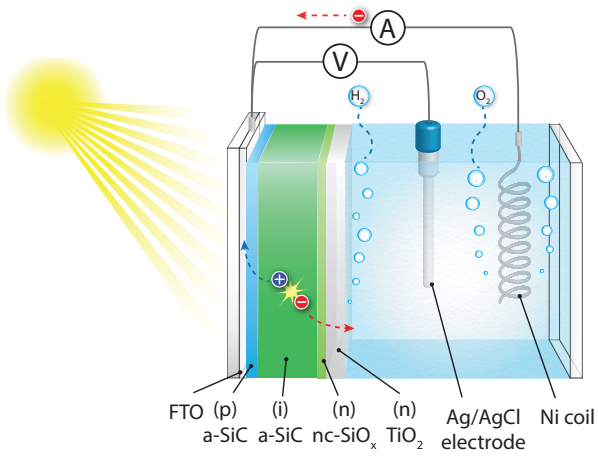

Fig. 1 Schematic photoelectrochemical setup used in this work including the a-SiC/TiO_2 working electrode and a Ni coil counter electrode in an alkaline (pH 14) electrolyte.

Material characterization

The morphology of the samples were characterized using a high-resolution scanning electron microscope (SEM, FEI Verios 460) with a through the lens detector (TLD) for secondary electrons. SEM images were recorded using an accelerating voltage of 10 kV. The material composition was characterized using an X-ray photoelectron spectroscopy (XPS, Thermo Scientific K-alpha) equipped with an Al K-alpha X-ray source and a flood gun. The crystal structure of the samples were characterized using a Bruker D8 Advance X-ray diffractometer equipped with LynxEye linear detector in a Bragg-Brentano configuration, with a cobalt source (Co–Kα_1 $\lambda = 1.788965$ Å).

Results and discussion

Electrohemical activities of dual-catalysts

To examine the electrochemical activity of the hydrogen evolution catalysts (Ni, Ni–Mo, and Ni/Ni–Mo), each catalyst was deposited onto TiO_2 to measure the current-potential (j–V) characteristics in the dark. The Ni–Mo catalyst was first electrodeposited potentiostatically onto TiO_2 at an applied potential of -1.2 V vs. Ag/AgCl, resulting in the formation of uniformly dispersed nanoparticles with a mean size of 10 nm, and with an interparticle spacing distance of a few nanometers that, in some regions, form agglomerates (shown by scanning electron microscopy (SEM) images in Fig. 2 and more detailed images are shown in ESI,† Fig. S1). Fig. 3 shows that Ni–Mo has a negligible overpotential to generate current for the HER. However, the incomplete coverage of Ni–Mo on the TiO_2 surface leads to a low number of catalytically active sites, which reduces the rate of the reaction, shown by the low slope of current as more negative potentials are applied. This slow reaction is ascribed to the limited pathway of electron transfer that is restricted through only the surface region covered by the Ni–Mo particles, as illustrated in Fig. 3b. At very negative potentials, the low number of active sites causes a large number of electrons to accumulate at the interface between the TiO_2 layer and the Ni–Mo nanoparticles, and thus lowers the rate of charge transfer from the semiconductor to the electrolyte since TiO_2 itself has very low activity to drive the HER (Fig. 2, black curve).

To try to overcome the poor kinetics of the Ni–Mo catalyst, a thin Ni film (2 nm) was sputter-deposited on the TiO_2 layer before the electrodeposition of Ni–Mo. Pure Ni is known to be an active and stable electrode material for the HER in an alkaline environment, and is thus also investigated as a catalyst layer on top of TiO_2 in our study. Although Ni alone shows a relatively large thermodynamic overpotential (0.2 V), it has an immediate increase of current near the onset potential (defined as the potential required to achieve -100 μA/cm^{-2}) as a result of the homogeneous coverage of the sputtered Ni film on TiO_2. The activity of the catalyst was enhanced further by depositing Ni–Mo onto Ni. SEM images show that the deposition of Ni–Mo onto Ni results in compact agglomerates with a larger spacing distance and a nonuniform distribution of larger particles over the surface (ESI,† Fig. S1). However, the insertion of a thin Ni can fill the interparticle gap of Ni–Mo particles that will subsequently increase

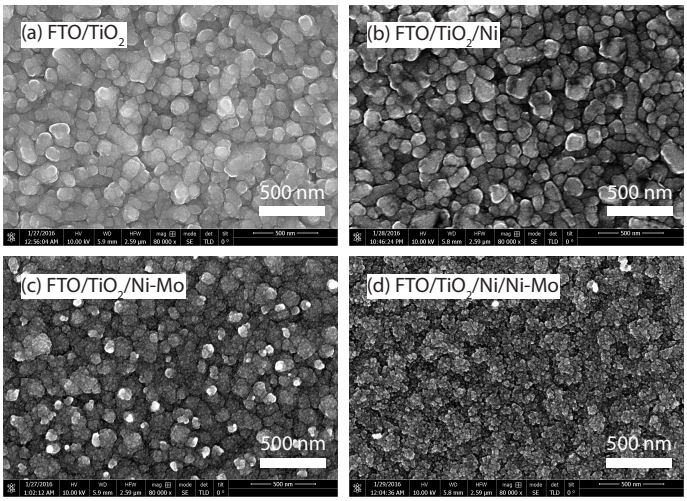

Fig. 2 Top-view SEM images of (a) FTO/TiO_2, (b) FTO/TiO_2/Ni, (c) FTO/TiO_2/Ni–Mo, (d) FTO/TiO_2/Ni/Ni–Mo.

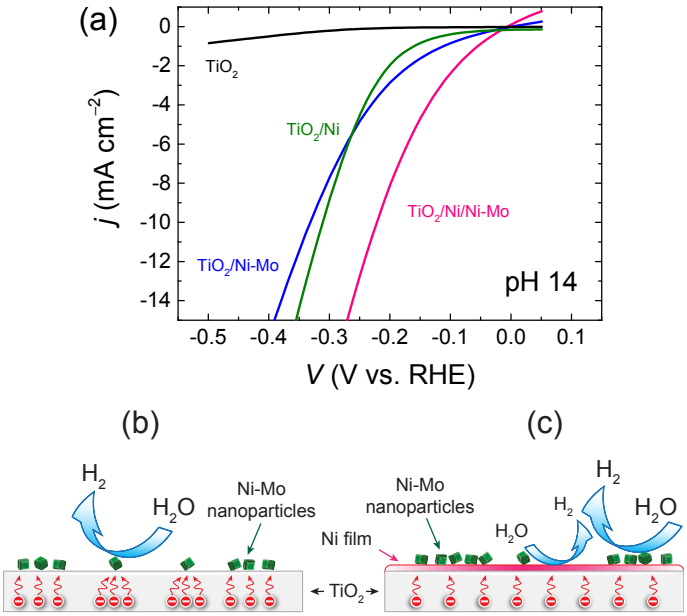

Fig. 3 (a) Linear sweep voltammetry of Ni, Ni–Mo, and Ni/Ni–Mo on TiO_2. All samples were measured in 1 M KOH at pH 14.(b) Schematic illustration of electron pathways through the catalytically active sites of Ni–Mo particles and (c) Ni/Ni–Mo dual-catalysts.

the number of HER active sites, and therefore allow electrons to transfer across the entire surface, as illustrated in Fig. 3c. Additionally, the Ni/Ni–Mo composite indirectly creates a synergistic effect that drives the reaction at a low overpotential while still maintaining the fast rate of the reaction. This is evidenced by the ability of Ni/Ni–Mo to rapidly increase the cathodic current near the same onset potential as that of only Ni–Mo, and produces higher current at more negative potentials. To give an illustration, the Ni–Mo requires an extra potential of 130 mV to achieve the same current density of -10 mA cm^{-2} that the Ni/Ni–Mo dual-catalyst needs.

Band-edge energetics of the interfacial layers

To understand the interfacial energetics between the TiO_2 layer, the catalyst and/or the electrolyte, electrochemical impedance spectroscopy (EIS) was performed in the dark in 1 M KOH electrolyte at pH 14. Representative Nyquist plots of each configuration are shown in Fig. 4a. Although the EIS of the bare TiO_2 was recorded over a frequency range from 100 kHz to 0.1 Hz, the analysis was only performed in the high-frequency region (*i.e.*, between 100 kHz and 50 Hz) where capacitive response in this region was prominent. Therefore impedance data can be modelled using a simple Randles circuit consisting of a series resistance of the electrolyte and electrical back contact (R_{series}), and a bulk resistance of TiO_2 that is related to exchange of electrons between the conduction band and electronic states on the surface (in this case the surface states) (R_{bulk})[28,29] in parallel with a space-charge capacitance of TiO_2 (C_{SC}), as shown in Fig. 4b. The complete data scan can be found in ESI,† Fig. S2. Adding extra components and using a more complex electronic circuit would allow for more accurate fittings of the impedance data, particularly in the low frequency region to account for processes occurring at the semiconductor/electrolyte interface, arisen by the Helmholtz layer. However, we noticed that the high-frequency response was somewhat overlapping with the low-frequency response in the Nyquist plot, corresponding to the space-charge layer and Helmholtz layer, respectively. Consequently, no distinct semicircles could be observed to discriminate each contribution. Taking all these individual processes into account in the equivalent circuit would inevitably lead to ambiguous interpretation, and therefore separating non-relevant contributions from the space-charge layer becomes even more complicated. To avoid this complexity, fitting impedance data was restricted to only region dominated by the space-charge layer (*i.e.*, typically between 100 kHz and 100 Hz) using a simple Randles circuit, thus allowing identification and determination of solely the C_{SC} of TiO_2.

Besides the Nyquist plot, additional valuable information of the EIS results can be obtained from the Bode phase plot shown in Fig. 5b. In this Bode phase plot, the TiO_2/electrolyte system exhibits phase angles lower than $-90°$, which is typically ascribed to a non-ideal capacitive behavior. Therefore, a constant phase element of the space-charge layer (CPE_{SC}) is used instead of the perfect C_{SC} element in the equivalent electronic circuit to fit the impedance data. The equivalent capacitance of a CPE is given by[30]

$$C = \mathrm{CPE}(\omega_{max})^{n-1} \quad (2)$$

where ω_{max} is the frequency at which the imaginary value of the impedance has the maximum, and n is the empirical constant that describes the electrical behavior of CPE, and can range between 0 (purely resistive) and 1 (purely capacitive). In a circuit model where the CPE is in parallel with R, the true capacitance can be estimated using the following relationship:[31]

$$C = R^{(1-n/n)}\mathrm{CPE}^{(1/n)} \quad (3)$$

The origin of this CPE behavior is most likely due to the presence of multiple surface states and/or deep impurity states with energy levels distributed within the band gap.[32]

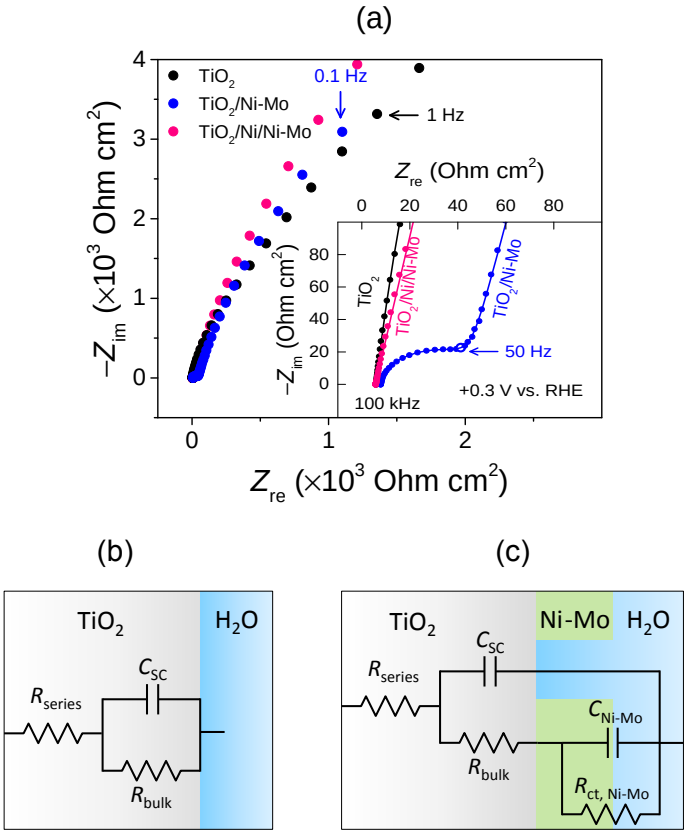

Fig. 4 (a) Nyquist plots of TiO_2 with and without the catalysts at +0.3 V *vs.* RHE. The horizontal axis is the real part of impedance (Z_{re}) and the vertical axis is the imaginary part of impedance (Z_{im}). The inset shows the magnification of the impedance response in the high-frequency region. The symbols represent the impedance data points from the EIS measurements and the solid lines represent the fit results using the equivalent electronic circuits. (b) Randles circuit used when one semicircle in the Nyquist plot is observed. (c) Equivalent circuit used when two semicircles are apparent, involving the contribution from the Ni–Mo catalyst.

When the Ni–Mo catalyst is deposited onto TiO_2, two-semicircle features in the Nyquist plot are apparent. The first semicircle (shown in the inset of Fig. 4a) in the high-frequency region is related to the contribution from the space-charge layer of TiO_2 and the low-frequency semicircle is associated with the contribution from the Ni–Mo catalyst. Consequently, extra components the constant phase element of Ni–Mo ($CPE_{Ni–Mo}$) and the charge transfer resistance of Ni–Mo ($R_{ct,\ Ni–Mo}$) are added to the equivalent circuit to interpret the impedance data, as shown in Fig 4c. The validity of this circuit was verified by independent investigation of the high-frequency response of the impedance data (*i.e.*, low semicircle); the obtained capacitances of the TiO_2/Ni–Mo from the fitted high-frequency impedance reveal identical values (in the same order of magnitude) as that of the bare TiO_2 throughout the whole potential range of measurement, as shown in Fig. 6a. Since the high-frequency impedance of a semiconductor is generally attributed to the contribution of the C_{SC}, this implies that the space-charge layer of the TiO_2 is not affected by the presence of Ni–Mo particles, and therefore the TiO_2 still forms

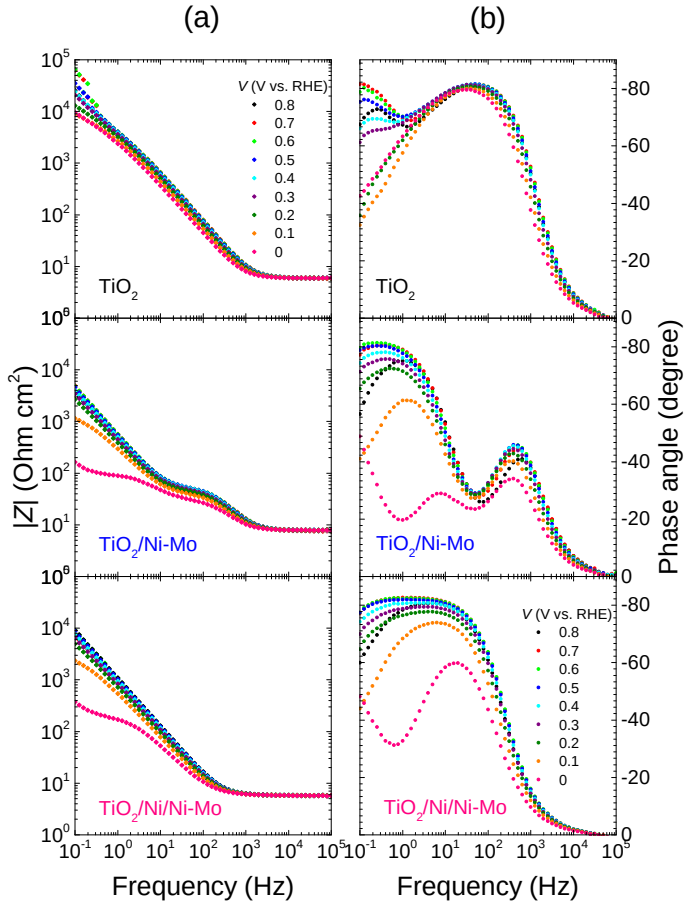

Fig. 5 Bode plots of (a) total impedance ($|Z|$) and (b) phase angle of TiO_2 with and without and the catalysts collected during EIS measurements at different applied potentials.

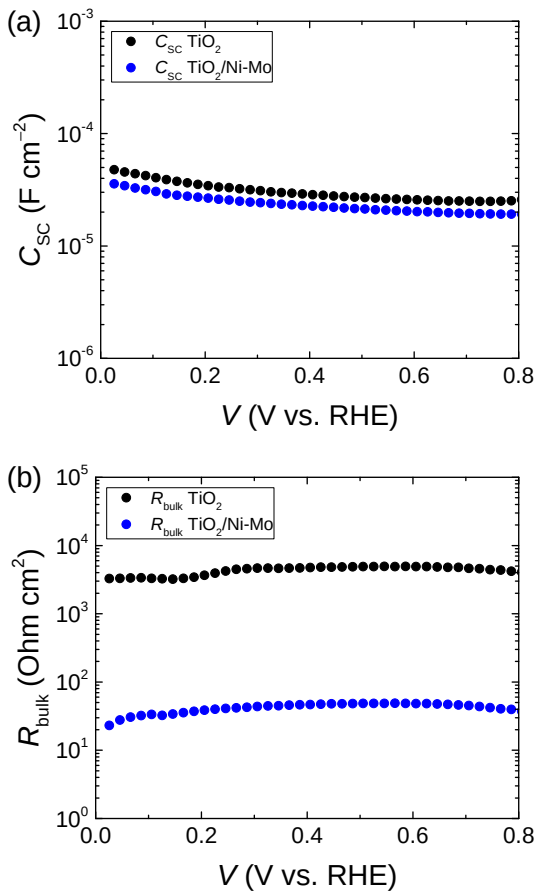

Fig. 6 (a) C_{SC} and (b) R_{bulk} of the TiO_2 in the bare TiO_2 (black circles) and TiO_2/Ni–Mo (blue circles) configurations. Values are obtained by fitting the impedance data with the equivalent circuits.

a solid/liquid junction with the electrolyte. The existence of the C_{SC} of the TiO_2 is also evidenced by the distinguishable peaks of phase angle in the high-frequency region (*i.e.*, 1 kHz) in the Bode phase plot (Fig. 5b), in addition to the broad phase-angle peaks in the low-frequency regime (10 Hz to 0.1 Hz). Another reason that allowed us to use this equivalent circuit was the fitting results of R_{bulk} of the TiO_2/Ni–Mo having lower values than that of the bare TiO_2 (Fig. 6b). This means that the exchange of electrons occur predominantly between the TiO_2 conduction band and the metallic Ni–Mo that have higher electron density than the TiO_2 surface state, and therefore lowering the resistance. To account for this process, the R_{bulk} element is in parallel association with $CPE_{Ni–Mo}$ and $R_{ct,\ Ni–Mo}$. This equivalent circuit allowed us to accurately fit the impedance data throughout the whole frequency range of measurement (ESI,† Fig. S3).

When a thin Ni film (2 nm) is introduced between the TiO_2 and Ni–Mo nanoparticles, the EIS data reveal only one semicircle in the Nyquist plot (Fig. 4a). Although the TiO_2/Ni/Ni–Mo exhibits a seemingly identical semicircle as that of the bare TiO_2, a careful examination in the Bode plot shows a clear shift of the onset of the total impedance ($|Z|$) from 2 kHz in for the bare TiO_2 to 200 Hz for the TiO_2/Ni/Ni–Mo (Fig. 5a). This means that the TiO_2/Ni/Ni–Mo has a nearly constant impedance in the high-frequency region (100 kHz to 200 Hz). In this frequency range, the $|Z|$ is almost equal to the real impedance (Z_{re}, *i.e.*, resistance, R) because the imaginary impedance (Z_{im}, *i.e.*, $1/\omega C$) is too insignificant such that its contribution to the $|Z|$ is negligible (ESI,† Fig. S4). This is also consistent with the zero or small phase angle observed from the TiO_2/Ni/Ni–Mo within the frequency range between 100 kHz and 200 Hz, contrary to the bare TiO_2 of which the phase angle peak is already observed at 100 Hz (Fig. 5b). This implies that the capacitive behavior of the TiO_2/Ni/Ni–Mo in the high frequency region is not present. Since the high-frequency impedance is generally attributed to the contribution from the electrical characteristic of the space-charge layer of the semiconductor, the constant response of impedance in the high-frequency region, thus the absence of C_{SC}, explicitly suggests that the electrical junction between TiO_2 and Ni is entirely dominated by the resistive behavior. This situation is likely due to the formation of an ohmic contact between TiO_2 and Ni whose work functions are nearly identical (5.1 eV for TiO_2 [33] and 5.04–5.35 eV for Ni [34]). A previous investigation using operando X-ray photoelectron spectroscopy (XPS) in a photoelectrochemical cell has also revealed that an ultrathin film of Ni is sufficient to effectively maintain a constant electronic band structure of the TiO_2 closer to the flat-band potential across a wide potential range, thus providing an ohmic behavior instead of a rectifying junction. [35] This ohmic con-

tact across the whole surface can be evidently true as confirmed by the nearly uniform coverage of Ni (ESI,† Fig. S4). In a strongly alkaline electrolyte, the thin Ni will oxidize to form nickel hydroxide, but will transform back to Ni at reductive potentials and is stable in the metallic form under cathodic conditions (ESI,† Fig. S5). These electrochemical processes where the TiO_2 has an ohmic contact with the catalyst can be modelled using a Randles circuit consisting of a R_{series} that already includes the resistance of the bulk of the TiO_2 (*i.e.*, $R_{series} = R_{contact} + R_{electrolyte} + R_{bulk}$), the charge transfer from the Ni/Ni–Mo ($R_{ct,\ Ni/Ni–Mo}$) and the capacitance or CPE of the Ni/Ni–Mo ($CPE_{Ni/Ni–Mo}$). The fit results of the impedance data using this equivalent circuit can be found in ESI,† Fig. S6.

The fit results of the C_{SC} of the TiO_2 from the EIS data were then used to construct Mott–Schottky plots in order to analyze the influence of the HER catalysts on the flat-band potential of TiO_2 (shown in Fig. 7). The intercept between the extrapolated inverse square capacitance of the TiO_2 space-charge layer with the *x*-axis indicates the flat-band potential of TiO_2. The TiO_2 with and without Ni–Mo particles exhibits nearly the same flat-band potential as the bare TiO_2 (-0.2 V *vs.* RHE) with a slight deviation which is still in the acceptable margin of error. This band pinning is expected as the Ni–Mo particles do not completely cover the TiO_2 film, thus still allowing the underlying TiO_2 to be in contact with electrolyte, and forming a rectifying solid/liquid junction. In the case of TiO_2 coated with Ni/Ni–Mo, the high-frequency impedance is not present, and therefore the flat-band potential cannot be determined. Fitting the low-frequency impedance with a Randles circuit results in a very distinct slope of the Mott–Schotky plot compared to the other two configurations. Since the low-frequency impedance is mainly attributed to the capacitance of the catalyst, the Mott–Schottky result obtained by fitting the impedance data with the equivalent circuit does not reflect the flat-band potential of TiO_2.

Following the electrochemical characterization of the different catalyst layers on TiO_2, the composite layers were deposited in the same conditions on the a-SiC photocathodes to observe their ability to transfer photogenerated charges to drive the HER. The influence of the catalysts on the interfacial energetics of TiO_2-protected a-SiC photocathodes at the solid-liquid interface was investigated by performing open-circuit voltage (OCV) measurements in the dark and under illumination, and is shown in Fig. 8. The presence of the TiO_2 front layer is important to maintain the stability of the a-SiC photocathode during OCV measurements, since without TiO_2 the a-SiC photocathode undergoes rapid corrosion even under open-circuit conditions. The OCV in the dark represents the pinning of the Fermi level of the photocathode with an electronic state of the front layer and the change in OCV under illumination represents the quasi-Fermi level splitting that translates into the built-in photovoltage of the photocathode. Without any catalyst and without illumination, the Fermi level of the a-SiC photocathode equilibriates with the surface electronic state of the TiO_2 at $+0.46$ V *vs.* RHE. This dark OCV value measured at pH 14 turns out to be close to the previously reported OCV measurement of a-SiC/TiO_2 measured at pH 4 ($+0.5$ V *vs.* RHE),[9] implying that the energy level of the our amorphous TiO_2 surface state is almost independent of the electrolyte pH, with respect to water redox potentials. The addition of the Ni–Mo catalyst onto the a-SiC/TiO_2 does not lead to a noticable change of the dark OCV. This is mainly due to the fact that the TiO_2 interfacial layer still forms a solid/liquid junction with the electrolyte and therefore the equilibriation of the Fermi level is not substantially affected by the Ni–Mo nanoparticles on the surface. In the case of the Ni/Ni–Mo dual-catalyst on the a-SiC/TiO_2 photocathode, a new thermal equilibrium is established and the Fermi level of the photocathode is pinned to the new equilibrium surface potential of the outermost layer ,*i.e.,* Ni at $+0.7$ V *vs.* RHE in the dark. At this dark open-circuit condition, no solid/liquid junction is expected because the electrical behavior between TiO_2 and Ni is dictated by an ohmic contact. During the dark and illuminated OCV measurements, all the photocathodes show a photovoltage of 0.8 V, confirming that the addition of the catalysts does not

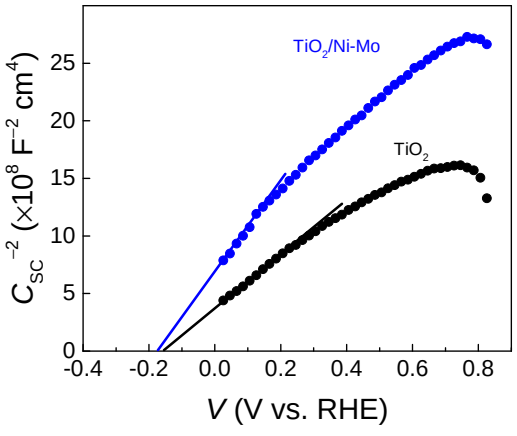

Fig. 7 Mott–Schottky plots of TiO_2 (100 nm) with (blue) and without Ni–Mo (black). The intercept between the extrapolated linear lines with the *x*-axis indicate the flat-band potentials. All measurements were performed in 1 M KOH pH 14.

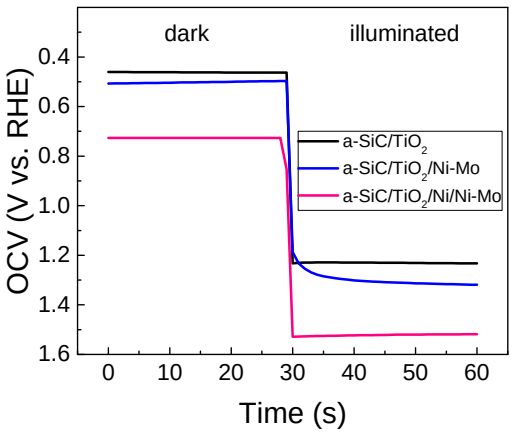

Fig. 8 Open-circuit voltage (OCV)measurements of the a-SiC/TiO_2 photocathode with and without the catalyst layers. The change in open-circuit voltage in the dark and under illumination represents the photovoltage of the composite systems.

affect the electronic equilibriation of the (p–i–n) structure of the a-SiC with the TiO_2, *i.e.*, that the buried junction photovoltage is maintained.

Photoelectrochemical activities of a-SiC photocathodes

The catalytic activities of Ni–Mo and Ni/Ni–Mo were further evaluated on a-SiC photocathodes by cyclic voltammetry under 1 sun illumination in a 1 M KOH electrolyte at pH 14, and the results are shown in Fig. 9. Without the catalysts, the TiO_2 protected a-SiC shows a late photocurrent onset potential (+0.2 V *vs.* RHE) due to the poor reaction kinetics on the bare TiO_2 surface. The addition of a Ni–Mo catalyst significantly shifts the onset potential, which can be closely seen from the intercept between the anodic and cathodic photocurrent at +0.8 V *vs.* RHE, shown in the inset of Fig. 9. This result is expected since at this onset potential, the constant photovoltage (0.8 V) of the buried junction a-SiC photocathode should allow the potential at the surface/electrolyte interface to be positioned at the hydrogen evolution potential (0 V *vs.* RHE), as illustrated in Fig. 10a. However, the photocurrent does not rise steeply at the onset potential, which is primarily due to the low number of active sites for hydrogen evolution of Ni–Mo on the photocathode. Accordingly, the maximum photocurrent density of the a-SiC photocathode with only a Ni–Mo HEC is limited to only -10 mA cm^{-2} at 0 V *vs.* RHE.

Cyclic voltammetry data in Fig. 9 also indicates that the photoelectrochemical activity of the a-SiC photocathode with Ni/Ni–Mo dual-catalyst is noticeably higher than that with only the Ni–Mo catalyst. A closer inspection in the inset of Fig. 9 reveals that both a-SiC photocathodes with Ni–Mo and Ni/Ni–Mo catalysts have the same onset potential of +0.8 V *vs.* RHE. Nevertheless, the instantaneous increase of photocurrent onset by the more efficient Ni/Ni–Mo dual-catalyst improves the photocurrent significantly throughout the whole potential range of measurement. Despite the increase of cathodic photocurrent, the anodic current of the a-SiC with Ni/Ni–Mo is also more profound at potentials more positive than +0.8 V *vs.* RHE. This anodic current is related to the oxidation of the exposed Ni catalyst to $Ni(OH)_3^-$ and the cathodic current at +0.9 V *vs.* RHE is associated with its reduction back to Ni. It is generally known from the Pourbaix diagram that the redox-phase transformation between Ni and $Ni(OH)_3^-$ in an extremely alkaline environment occurs at near the hydrogen evolution potential (ESI,† Fig. S7). The reduction and oxidation of Ni near the photocurrent onset potential at +0.8 V *vs.* RHE is also consistent with the constant photovoltage of a-SiC (0.8 V) that brings the surface potential of Ni to near the hydrogen evolution potential, thus allowing Ni to oxidize or reduce depending on the direction of the potential scan during cyclic voltammetry, as illustrated in Fig. 10b. At potentials more negative than +0.8 V *vs.* RHE, Ni is stable in the metallic form and performs the catalytic reaction of hydrogen evolution (Fig. 10c). The enhancement of the photoelectrochemical activity of a-SiC by an efficient Ni/Ni–Mo dual-catalyst leads to an increased photocurrent density of -14 mA cm^{-2} at 0 V *vs.* RHE. This is the highest reported photocurrent from amorphous-Si-based photoelectrodes for photoelectrochemical hydrogen evolution. This result is made even more impressive that the entire structure (a-SiC/TiO_2/Ni/Ni–Mo) is less than 150 nm, and composed entirely of earth abundant materials.

Stability of a-SiC photocathodes

The stability of our a-SiC photocathode under photoelectrocatalytic conditions was evaluated by performing chronoamperometry measurements at a fixed applied potential of 0 V *vs.* RHE, and the result is shown in Fig. 11. The a-SiC photocathode only shows a stable photocurrent for 40 minutes, followed by a rapid deactivation and sharp decrease of photocurrent, which leaves only 35% of the initial value after 1 hour. To confirm that the photocurrent was related to the hydrogen evolution reaction, the hydrogen was measured during the illuminated chronoamperometry experiment using a gas chromatography (GC). The time resolution of data collection of our GC is 18 minutes (the lowest

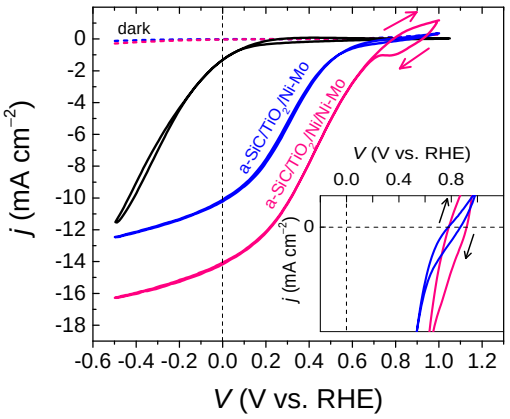

Fig. 9 Cyclic voltammetries of a-SiC/TiO_2 with Ni–Mo and Ni/Ni–Mo under 1 sun illumination. The inset shows the photocurrent onset potential of the photocathodes at +0.8 V *vs.* RHE. The measurements were performed in 1 M KOH at pH 14.

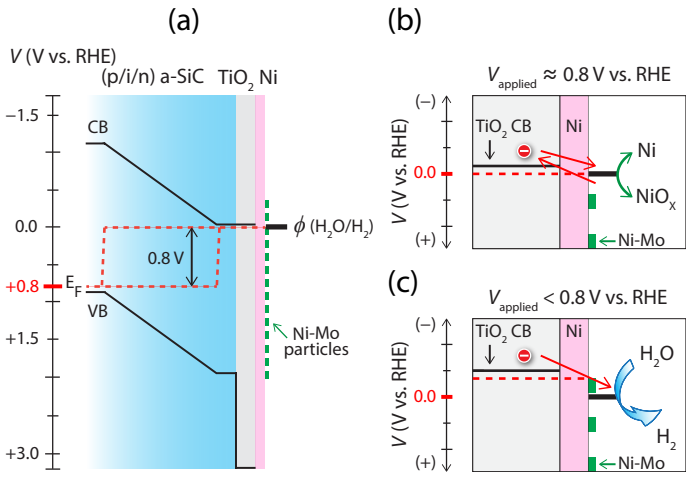

Fig. 10 (a) Energy band diagram at applied potential +0.8 V *vs.* RHE. Schematic illustration of (b) Ni oxidation and reduction at an applied potential on a-SiC of ≈ +0.8 V *vs.* RHE and (c) the position of surface potential at applied potentials on a-SiC of < +0.8 V *vs.* RHE.

time limit for our particular device). In order to accurately calculate the Faradaic efficiency, the current was integrated every 18 minutes to determine the total number of charge generated over the data collection time. This measurement allowed for quantification of evolved hydrogen gas and the rate of corrosion of the photocathode by photogenerated electrons. During the measurement, the Faradaic efficiency remained nearly 100% in the first 40 minutes, and exceeded unity (117%) when the photocurrent dropped steeply. The overestimated Faradaic efficiency is probably due to the dissolution of our hydrogenated a-SiC during the chronoamperomety measurements that released hydrogen, and was detected by the GC. The origin of the decay of photocurrent may be caused by the instability of the TiO_2 protection layer under very cathodic applied bias or the presence of pinholes in TiO_2 that exposes a-SiC to the highly corrosive electrolyte (1 M KOH), and subsequently etches the a-SiC. As the thickness of the photocathode is reduced, the number of photogenerated electron decreases, causing the photocurrent to drop. Without the TiO_2 layer, the a-SiC dissolves faster even in the dark, in the same electrolyte solution and without applied bias (*i.e.,* no net current flow), leaving only the FTO after 1 hour (ESI,† Fig. S8). This confirms that the a-SiC photocathode is intrinsically unstable when exposed to a strongly alkaline environment.

In order to confirm the durability of our TiO_2 protection layer, a separate stability experiment was performed using only TiO_2 on FTO (without the a-SiC photocathode) and using the different catalyst configurations. From the chronopotentiometry measurement in the dark at a fixed current of -10 mA cm^{-2}, all catalyzed FTO/TiO_2 samples demonstrate a good stability for 24 hours and were able to maintain a potential more positive than -0.5 V *vs.* RHE (ESI,† Fig. S9). To confirm the stability of the TiO_2, an XPS analysis was performed on the Ni-catalyzed TiO_2 before and after the stability test. The thin Ni film was chosen instead of the Ni/Ni–Mo dual-catalyst because the 2 nm of Ni should allow the photoelectron from TiO_2 to escape and be detected by the XPS, since the escape depth is typically in the range of 3 and 4 nm. Before the stability measurement, the Ti 2*p* signal from TiO_2 was weak because it was covered by Ni (ESI,† Fig. S10). XPS data reveal that the Ti 2*p* signal is still detectable after 24 hours, which means that TiO_2 was not dissolved, and remained present after the test. Interestingly, the Ti 2*p* signal becomes stronger after 24-hour measurement. This is probably because of the detachment of Ni from TiO_2 during the long chronoamperometry test. The removal of Ni is also observed from the reduced intensity of Ni 2*p* signals in the XPS data and the increased intensity of Ti 2*p* signal after prolonged testing, which indicates TiO_2 became uncovered and more detectable due to the disappearance of the Ni film (ESI,† Fig. S11).

In the case of TiO_2 as a protection layer for the a-SiC photocathode, degradation of the photocurrent still occurs even at lower applied potential (+0.3 V *vs.* RHE, ESI,† Fig. S12). Many reports have attributed the failure of a TiO_2 protection layer to electron trapping in TiO_2 that reduces Ti^{4+} to Ti^{3+} states along with proton intercalation that affects the compositional, structural and physical changes of TiO_2 which subsequently results in deactivation of TiO_2 as an electron transporting layer.[36,37] However in the highly alkaline solution (1 M KOH), the concentration of protons is too insignificant for intercalation to occur. Visual examination reveals that the rapid decay of photocurrent is mainly due to the dissolution of a-SiC. Since in our experiment the catalyzed TiO_2 alone is stable under moderate potential bias (more positive than -0.5 V *vs.* RHE, shown in ESI,† Fig. S9), we therefore speculate that the corrosion of a-SiC takes place because of the diffusion of hydroxide ions through TiO_2 that can reach further to the unprotected a-SiC, and results in corrosion. This ionic diffusion in TiO_2 most likely occurs due to the open structure and/or the presence of pinholes of the thin amorphous oxide produced by low-temperature ALD. In the case of our stability measurement using TiO_2 film on FTO, hydroxide ions can still diffuse. However, since the FTO underneath is more chemically stable, the ionic diffusion does not affect the durability of the whole composite system, and thus we do not observe any substantial degradation. Very recently, Bae *et. al.* reported that the pinholes within TiO_2 could result in the permeation of the highly concentrated KOH, which causes corrosion in the underlying Si photocathode.[38]

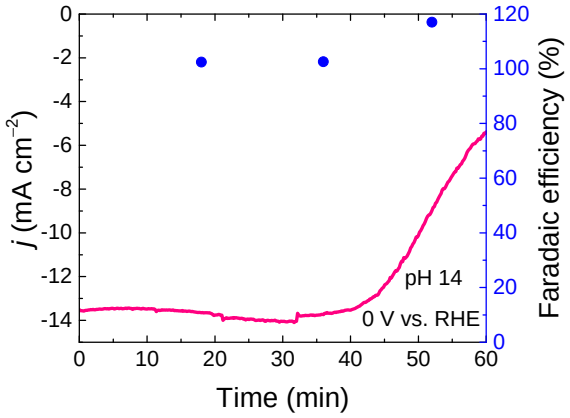

Fig. 11 Chronoamperometry measurement of TiO_2 coated a-SiC photocathodes with Ni/Ni–Mo catalyst at a fixed potential of 0 V *vs.* RHE.

Several efforts have been attempted to use amorphous TiO_2 as the protection layer for photocathodes in a strongly alkaline environment, yet similar failures were obtained after a few hours.[8,39] This likely implies that although amorphous TiO_2 may be an excellent passivation material in a near neutral environment,[40] it may be unsuitable as a protection layer for photocathodes in a strongly alkaline electrolyte. Numerous studies suggest that corrosion protection by TiO_2 is mostly effective in its compact crystalline form.[4,37,38] Transforming the amorphous structure of TiO_2 to a crystalline phase may require in-situ or post-annealing at temperatures of at least 400 °C. Our a-SiC, however, cannot survive at this extreme temperature (ESI,† Fig. S13), and therefore the post-annealing procedure was limited to only 300 °C. This temperature is evidently insufficient to improve the amorphous TiO_2 to its crystalline form, as suggested by the absence of TiO_2 peaks in the X-ray diffraction pattern (ESI,† Fig. S14). Several reports have demonstrated that deposition of crystalline TiO_2 by low-temperature ALD is indeed possible even without annealing treatement.[41,42] In our future work, a similar approach will be tried to maintain the high performance and improve the stability

of a-SiC photocathodes in an alkaline solution.

Conclusions

In summary, we have demonstrated a significant improvement of the activity of a Ni–Mo catalyst by incorporating a thin Ni film on TiO_2 coated a-SiC photocathodes prior to Ni–Mo electrodeposition, which results in a dramatic increase of photocurrent up to -14 mA cm^{-2} at 0 V *vs.* RHE in an alkaline solution. The dual-catalyst enhances the photocurrent by increasing the number of active site for catalysis, thus allowing electron to transfer in a large area and preventing charge accumulation on the surface. Additionally, using EIS and Mott–Schottky analysis, we investigated the rectifying junction behavior between TiO_2 and electrolyte in the presence of Ni–Mo nanoparticles and the removal of the solid/liquid junction to form an ohmic contact when thin Ni film is added using magnetron sputtering before the electrodeposition of Ni–Mo. This work shows the potential of a Ni/Ni–Mo dual-catalyst as an efficient electrocatalyst for photocathodes and reveals the importance of high surface coverage of catalysts on the photoelectrochemical activity of the photoelectrodes. The high activity of the Ni/Ni–Mo dual-catalyst should motivate the utilization of dual-catalysts on photoelectrodes to maximize the photocurrent output for hydrogen evolution.

Acknowledgements

The authors would like to thank Prof. Bernard Dam for helpful discussion, Joost Middelkoop, Herman Schreuders and Stefaan Heirman for technical support, and Bartek Trześniewski for the assistance with XPS analysis. This work is part of the research programme of the Foundation for Fundamental Research on Matter (FOM), which is part of the Netherlands Organization for Scientific Research (NWO) and is financed by the BioSolar Cells open innovation consortium (W. A. Smith and I. A. Digdaya), supported by the Dutch Ministry of Economic Affairs, Agriculture and Innovation. Financial support from the APPEL project (granted to A. H. M. Smets and W. A. Smith) by NWO/FOM/Shell is gratefully acknowledged. E. C. Garnett and G. W. P. Adhyaksa acknowledge support from an ERC starting grant "NanoEnabledPV", grant number 337328.

References

1 M. Zeman, *Advanced Amorphous Silicon Solar Cell Technologies*, John Wiley & Sons, Ltd, Chichester, 2006, pp. 173–236.

2 A. Madan and M. P. Shaw, *The Physics and Applications of Amorphous Semiconductors*, Academic Press, Inc., London, 1988.

3 L. Han, I. A. Digdaya, T. W. F. Buijs, F. F. Abdi, Z. Huang, R. Liu, B. Dam, M. Zeman, W. A. Smith and A. H. M. Smets, *J. Mater. Chem. A*, 2014, **3**, 1–8.

4 B. Seger, T. Pedersen, A. B. Laursen, P. C. K. Vesborg, O. Hansen and I. Chorkendorff, *J. Am. Chem. Soc.*, 2013, **135**, 1057–1064.

5 Y. W. Chen, J. D. Prange, S. Dühnen, Y. Park, M. Gunji, C. E. D. Chidsey and P. C. McIntyre, *Nat. Mater.*, 2011, **10**, 539–544.

6 S. Hu, M. R. Shaner, J. A. Beardslee, M. Lichterman, B. S. Brunschwig and N. S. Lewis, *Science*, 2014, **344**, 1005–1009.

7 Y. Lin, C. Battaglia, M. Boccard, M. Hettick, Z. Yu, C. Ballif, J. W. Ager and A. Javey, *Nano lett.*, 2013, **13**, 5615–5618.

8 C. G. Morales-Guio, K. Thorwarth, B. Niesen, L. Liardet, J. Patscheider, C. Ballif and X. Hu, *J. Am. Chem. Soc.*, 2015, **137**, 7035–7038.

9 I. A. Digdaya, L. Han, T. W. F. Buijs, M. Zeman, B. Dam, A. H. M. Smets and W. A. Smith, *Energy Environ. Sci.*, 2015, **8**, 1585–1593.

10 E. Kemppainen, A. Bodin, B. Sebok, T. Pedersen, B. Seger, B. Mei, D. Bae, P. C. K. Vesborg, J. Halme, O. Hansen, P. D. Lund and I. Chorkendorff, *Energy Environ. Sci.*, 2015, **8**, 2991–2999.

11 D. Merki, S. Fierro, H. Vrubel and X. Hu, *Chem. Sci.*, 2011, **2**, 1262–1267.

12 D. Merki, H. Vrubel, L. Rovelli, S. Fierro and X. Hu, *Chem. Sci.*, 2012, **3**, 2515–2525.

13 P. D. Tran, S. S. Pramana, V. S. Kale, M. Nguyen, S. Y. Chiam, S. K. Batabyal, L. H. Wong, J. Barber and J. Loo, *Chem. Eur. J.*, 2012, **18**, 13994–13999.

14 P. D. Tran, S. Y. Chiam, P. P. Boix, Y. Ren, S. S. Pramana, J. Fize, V. Artero and J. Barber, *Energy Environ. Sci.*, 2013, **6**, 2452–2459.

15 D. Voiry, H. Yamaguchi, J. Li, R. Silva, D. C. B. Alves, T. Fujita, M. Chen, T. Asefa, V. B. Shenoy, G. Eda and M. Chhowalla, *Nat. Mater.*, 2013, **12**, 850–855.

16 E. J. Popczun, J. R. McKone, C. G. Read, A. J. Biacchi, A. M. Wiltrout, N. S. Lewis and R. E. Schaak, *J. Am. Chem. Soc.*, 2013, **135**, 9267–9270.

17 L. Feng, H. Vrubel, M. Bensimon and X. Hu, *Phys. Chem. Chem. Phys.*, 2014, **16**, 5917–5921.

18 M. D. Scanlon, X. Bian, H. Vrubel, V. Amstutz, K. Schenk, X. Hu, B. Liu and H. H. Girault, *Phys. Chem. Chem. Phys.*, 2013, **15**, 2847–2857.

19 W.-F. Chen, C.-H. Wang, K. Sasaki, N. Marinkovic, W. Xu, J. T. Muckerman, Y. Zhu and R. R. Adzic, *Energy Environ. Sci.*, 2013, **6**, 943–951.

20 P. C. K. Vesborg, B. Seger and I. Chorkendorff, *J. Phys. Chem. C*, 2015, **6**, 951–957.

21 C. C. L. McCrory, S. Jung, J. C. Peters and T. F. Jaramillo, *J. Am. Chem. Soc.*, 2013, **135**, 16977–16987.

22 I. A. Raj and K. I. Vasu, *J. Appl. Electrochem.*, 1992, **22**, 471–477.

23 C. Fan, D. L. Piron, A. Sleb and P. Paradis, *J. Electrochem. Soc.*, 1994, **141**, 850–855.

24 W.-F. Chen, K. Sasaki, C. Ma, A. I. Frenkel, N. Marinkovic, J. T. Muckerman, Y. Zhu and R. R. Adzic, *Angew. Chem. Int. Ed.*, 2012, **51**, 6131–6135.

25 Y. Wang, G. Zhang, W. Xu, P. Wan, Z. Lu, Y. Li and X. Sun, *ChemElectroChem*, 2014, **1**, 1138–1144.

26 C. C. L. McCrory, S. Jung, I. M. Ferrer, S. Chatman, J. C. Peters and T. F. Jaramillo, *J. Am. Chem. Soc.*, 2015, **137**, 4347–4357.

27 J. R. McKone, E. L. Warren, M. J. Bierman, S. W. Boettcher, B. S. Brunschwig, N. S. Lewis and H. B. Gray, *Energy Environ.*

Sci., 2011, **4**, 3573–3583.

28 Z. Hens, *J. Phys. Chem. B*, 1999, **103**, 122–129.

29 L. Bertoluzzi and J. Bisquert, *J. Phys. Chem. Lett.*, 2012, **3**, 2517–2522.

30 C. H. Hsu and F. Mansfeld, *Corrosion*, 2001, **57**, 747–748.

31 M. E. Orazem, P. Shukla and M. A. Membrino, *Electrochim. Acta*, 2002, **47**, 2027–2034.

32 R. van de Krol and M. Grätzel, *Photoelectrochemical Hydrogen Production*, Springer US, Boston, MA, 2012, vol. 102.

33 D. O. Scanlon, C. W. Dunnill, J. Buckeridge, S. A. Shevlin, A. J. Logsdail, S. M. Woodley, C. R. A. Catlow, M. J. Powell, R. G. Palgrave, I. P. Parkin, G. W. Watson, T. W. Keal, P. Sherwood, A. Walsh and A. A. Sokol, *Nat. Mater.*, 2013, **12**, 798–801.

34 D. R. Lide, *CRC Handbook of Chemistry and Physics*, CRC Press, Boca Raton, FL, Internet V edn., 2005, p. 2005.

35 M. F. Lichterman, S. Hu, M. H. Richter, E. J. Crumlin, S. Axnanda, M. Favaro, W. Drisdell, Z. Hussain, T. Mayer, B. S. Brunschwig, N. S. Lewis, Z. Liu and H.-J. Lewerenz, *Energy Environ. Sci.*, 2015, **8**, 2409–2416.

36 A. Paracchino, V. Laporte, K. Sivula, M. Grätzel and E. Thimsen, *Nat. Mater.*, 2011, **10**, 456–461.

37 B. Seger, D. S. Tilley, T. Pedersen, P. C. K. Vesborg, O. Hansen, M. Grätzel and I. Chorkendorff, *RSC Adv.*, 2013, **3**, 25902–25907.

38 D. Bae, S. Shayestehaminzadeh, E. B. Thorsteinsson, T. Pedersen, O. Hansen, B. Seger, P. C. K. Vesborg, S. Ólafsson and I. Chorkendorff, *Sol. Energy Mater. Sol. Cells*, 2016, **144**, 758–765.

39 C. G. Morales-Guio, L. Liardet, M. T. Mayer, S. D. Tilley, M. Grätzel and X. Hu, *Angew. Chem. Int. Ed.*, 2014, 664–667.

40 J. Azevedo, L. Steier, P. Dias, M. Stefik, C. T. Sousa, J. P. Araújo, A. Mendes, M. Graetzel and S. D. Tilley, *Energy Environ. Sci.*, 2014, **7**, 4044–4052.

41 A. K. Chandiran, A. Yella, M. Stefik, L.-P. Heiniger, P. Comte, M. K. Nazeeruddin and M. Grätzel, *ACS Appl. Mater. Interfaces*, 2013, **5**, 3487–3493.

42 M. Reiners, K. Xu, N. Aslam, A. Devi, R. Waser and S. Hoffmann-Eifert, *Chem. Mater.*, 2013, **25**, 2934–2943.